

Article

Synthesis of g-C₃N₄ Derived from Different Precursors for Photodegradation of Sulfamethazine under Visible Light

Ke Li ^{1,2}, Miaomiao Chen ¹, Lei Chen ^{1,*}, Songying Zhao ¹, Wencong Xue ¹, Zixuan Han ¹ and Yanchao Han ²

¹ Key Laboratory of Song Liao Aquatic Environment, Ministry of Education, Jilin Jianzhu University, Changchun 130118, China

² State Key Laboratory of Electroanalytical Chemistry, Changchun Institute of Applied Chemistry, Chinese Academy of Sciences, Changchun 130022, China

* Correspondence: chenlei.jliae@hotmail.com

Abstract: In this study, a series of g-C₃N₄ nanosheets were prepared by various thermal oxidative etching times from four different precursors (urea, melamine, dicyandiamide and thiourea). The physicochemical properties of these g-C₃N₄ nanosheets were analyzed in detail using scanning electron microscopy (SEM), X-ray diffraction (XRD), photoluminescence emission spectra, Fourier transform infrared spectroscopy (FTIR), Brunauer–Emmett–Teller (BET) analysis and ultraviolet-visible diffuse reflectance. The results revealed that the g-C₃N₄ nanosheets obtained a thinner layer thickness and larger specific surface area, with an extension of thermal oxidative etching time. Meanwhile, sulfamethazine (SMZ), one of the most widely used sulfonamides, was used to evaluate the photocatalyst activity of the g-C₃N₄ nanosheets prepared in this study. Compared to other g-C₃N₄ nanosheets, urea-derived g-C₃N₄ nanosheets under 330 min thermal oxidative etching showed the highest photocatalytic activity for SMZ under visible light. In conclusion, our study provides detailed insights into the synthesis and characterization of g-C₃N₄ nanosheets prepared from various precursors and highlights the importance of thermal oxidative etching time in determining the photocatalytic activity of these materials.

Keywords: visible light; photocatalyst; g-C₃N₄; sulfonamides



Citation: Li, K.; Chen, M.; Chen, L.; Zhao, S.; Xue, W.; Han, Z.; Han, Y. Synthesis of g-C₃N₄ Derived from Different Precursors for Photodegradation of Sulfamethazine under Visible Light. *Processes* **2023**, *11*, 528. <https://doi.org/10.3390/pr11020528>

Academic Editor: Andrea Petrella

Received: 25 January 2023

Revised: 3 February 2023

Accepted: 7 February 2023

Published: 9 February 2023



Copyright: © 2023 by the authors. Licensee MDPI, Basel, Switzerland. This article is an open access article distributed under the terms and conditions of the Creative Commons Attribution (CC BY) license (<https://creativecommons.org/licenses/by/4.0/>).

1. Introduction

Antibiotics have been extensively used to treat infectious diseases in humans and domestic animals since the first antibiotic was deployed in 1910 [1–3]. Among these antibiotics, sulfonamide, a class of antibiotics which contains sulfonamide groups, has been one of the most widely used antibiotics in medical and animal livestock since 1968 [4]. Numerous sulfonamides are discharged into the aquatic environment through incomplete metabolism and wastewater treatment each year [5,6]. Sulfonamides may be harmful to the ecosystem and induce an antimicrobial resistance crisis after enough time has passed [7,8]. However, sulfonamides cannot be removed effectively through conventional biological wastewater treatment owing to their antibacterial nature [9]. Six kinds of sulfonamide were detected in the Pearl River Delta, which received effluents from four nearby typical wastewater treatment plants, demonstrating that the wastewater treatment plants cannot completely remove sulfonamides in the influent [10]. García-Galán et al. made use of removal rates and half-lives to study the rate of sulfonamides in the influent and effluent from 22 conventional wastewater treatment plants, 15 of which involved sewage. The results showed that even increasing hydraulic retention time could not increase the removal rate of sulfonamides, while sulfamethoxazole, sulfapyridine and their corresponding acetylated metabolites were detected most frequently and at very high concentrations [11]. Thus, finding an effective way to remove sulfonamides from surface water is essential to protect human health and guarantee ecology security.

Thus far, numerous technologies have been employed to solve sulfonamide contamination, such as adsorption [12,13], electrolysis [14], membrane separation [15], biological treatment [16], chemical catalysts [17,18] and photocatalysis [9]. Azhar et al. successfully synthesized a metal–organic framework adsorptive with high surface area and unsaturated metal sites through a facile method, which could totally remove sulfachloropyridazine from wastewater within 15 min due to its significant adsorption capacity [19]. Zhang et al. constructed an in situ electro-Fenton system to degrade sulfadiazine from simulated livestock and poultry breeding wastewater, and found that 96.5% of sulfadiazine could be removed in 150 min by this system when the pH value equals 3, the Pd/CeO₂ catalyst dosage is 0.1 g, the current density is 15 mA/cm², and the current ratio is 0.15:0.02 [20]. Liang et al. built an integrated membrane filtration consisting of ultrafiltration and two-stage reverse osmosis to remove antibiotic resistance genes mainly induced by sulfonamides from swine wastewater, and discovered that more than 99.79% of antibiotic resistance genes could be reduced by the integrated membrane filtration [21]. Yu et al. constructed an aerobic submerged membrane bioreactor integrating sponge-plastic biocarriers and successfully applied it to the degradation of sulfadiazine and sulfamethoxazole [22]. Li et al. investigated the use of surface molecular imprinting technology to remove sulfonamides, and the result revealed that the catalyst capacity for sulfamethazine (SMZ) and sulfathiazole reached more than 70% and 87%, respectively [23]. Among these technologies, photocatalysis has been revealed to be a promising method of removing sulfonamides and other organic contaminants because it is efficient, costly and environmentally friendly [24–26]. The photocatalysis process should be driven by light irradiation, and visible light accounts for 45% of solar sunlight, while only 5% of sunlight is UV light [27]. Therefore, it is very important to determine whether visible light can be utilized for photocatalyst technology. Over past years, graphitic carbon nitride (g-C₃N₄) has exhibited great potential to be applied in visible light photocatalysis because it can absorb visible light due to its band gap of 2.70 eV [28]. Additionally, g-C₃N₄ possesses many advantages, such as physicochemical stability, cost-effectiveness, easy synthesis, material abundance and environmental friendliness [29–31]. However, it is worth noting that bulk g-C₃N₄ shows lower catalytic activity due to its fast photogenerated charge recombination, low specific surface area, and weak oxidation-reduction ability. In general, the bands associated with steep edges are caused by electronic excitations from the valence band (VB) to the conduction band (CB), while those associated with weak visible light absorption are caused by incomplete long-range order in the atomic structure caused by tail excitation [32,33]. Hence, to obtain better catalytic performance, it is necessary to optimize the structure of g-C₃N₄ to improve the quantum size effect [34]. At present, there are many methods of improving the visible light catalytic activity of g-C₃N₄, including the preparation of surface sensitization, metal or non-metal doping, and heterojunctions with other photocatalysts [24,35–38]. Putri et al. doped oxygen atoms to bulk g-C₃N₄ through the hydrothermal method with H₂O₂ at 120 °C. The result showed that the specific surface area of g-C₃N₄ increased from 75 to 85 m²·g^{−1} because of the presence of the O element, which can enhance photocatalyst activity significantly [39]. Yan et al. successfully doped metal elements, such as Mg, K, Ca and Na, to g-C₃N₄ derived from urea, and found that the doped metal atoms junking with O atoms would change the photocatalyst morphology and electronic structures, which can improve the photocatalyst absorption capacity of visible light and decrease photogenerated charge recombination rate [40]. Li et al. synthesized and characterized g-C₃N₄/Bi₂MoO₆ heterojunctions, and the results suggested that the photocatalytic efficiency of g-C₃N₄/Bi₂MoO₆ was more than three times that of pristine g-C₃N₄ or Bi₂MoO₆ [41].

Many studies have proven that the morphology of g-C₃N₄ nanostructures is essential for photocatalysis performance [42]. Exfoliating bulk g-C₃N₄ into nanosheets has been proven to enhance its photocatalytic activity through thermal oxidative etching [43,44]. Meanwhile, the length of thermal oxidative etching time plays a key role in the microstructure and surface chemistries of g-C₃N₄ [45,46]. Moreover, g-C₃N₄ synthesized from various

precursors also has different photocatalytic activities [30,46]. Therefore, it is also crucial to choose the proper precursor to improve the photocatalytic performance of $g\text{-C}_3\text{N}_4$.

In this study, bulk $g\text{-C}_3\text{N}_4$ was first synthesized by using urea, melamine, dicyandiamide and melamine, respectively, as precursors. Then, $g\text{-C}_3\text{N}_4$ with different surface morphologies and sizes were directly synthesized via thermal oxidative etching of bulk $g\text{-C}_3\text{N}_4$ in air for various periods of time. Next, the physiochemical properties of the different bulk $g\text{-C}_3\text{N}_4$ derived from various precursors, and their corresponding $g\text{-C}_3\text{N}_4$ through thermal oxidative etching, were then analyzed according to the characterization results. SMZ, one of the most widely used sulfonamides, was chosen as a model contaminant substance to evaluate the photocatalytic activities of $g\text{-C}_3\text{N}_4$ derived from various precursors under visible sunlight. This paper focuses on the different precursors, as well as the impact of the thermal oxidative etching time on the structure and photocatalytic performance.

2. Experimental

2.1. Materials

Urea, melamine, dicyandiamide and thiourea for this experiment were obtained from Tianjin Xintong Fine Chemicals Company Limited, Tianjin, P. R. China. SMZ was obtained from Shanghai McLean Biochemical Technology Co., Ltd., Shanghai, P. R. China. All chemicals used in this study were analytical grade and used without further purification. All solutions were prepared using deionized water.

2.2. Synthesis of $g\text{-C}_3\text{N}_4$ Samples

The $g\text{-C}_3\text{N}_4$ samples were synthesized by a thermal oxidative etching method using urea, melamine, dicyandiamide and thiourea, respectively [43]. Briefly, the bulk $g\text{-C}_3\text{N}_4$ sample prepared from urea was synthesized as follows: 10 g of urea was put into a semi-closed crucible with a cover and calcined at 550 °C for 4 h with a heating rate of 2 °C min⁻¹ in a muffle furnace. After the thermal treatment, the obtained yellow-colored powder was cooled to room temperature naturally, then washed thoroughly with distilled water and ethanol, and then dried at 60 °C for 12 h and denoted as U0. Other precursors (melamine, dicyandiamide and thiourea) were also used to synthesize bulk $g\text{-C}_3\text{N}_4$ samples by a similar method, and the synthesized samples were denoted as M0, D0 and T0, respectively. U0 was calcined at 500 °C for 165 min or 330 min with a heating rate of 5 °C min⁻¹ in a muffle furnace; the resulting products were denoted as U165 and U330, respectively. M0, D0 and T0 were also used to synthesize $g\text{-C}_3\text{N}_4$ samples through a similar thermal oxidative etching method to that mentioned above and denoted as M165, M330, D165, D330, T165 and T330, respectively.

2.3. Characterization of the Synthesized $g\text{-C}_3\text{N}_4$

The surface morphologies and microstructure properties of the $g\text{-C}_3\text{N}_4$ samples were measured by a scanning electron microscope (SEM, FEI Quanta-PEG450, American FEI, USA). X-ray diffraction (XRD) patterns of the $g\text{-C}_3\text{N}_4$ samples were collected by an X-ray diffractometer (Rigaku UltimaIV, Japan), where the 2 θ values of the obtained data ranged from 10 to 90° with Cu K α irradiation. The photoluminescence (PL) properties of the $g\text{-C}_3\text{N}_4$ samples were measured using a F-98 system (Shanghai, China). XPS measurements were finished using a Thermo VG ESCALAB-250 (Thermo-VG Scientific, Waltham, MA, USA) under AlK α (1486.6 eV) radiation. The FTIR spectrum was obtained with a PerkinElmer Spectrum Two spectrometer (PerkinElmer Instruments Co., Ltd., Waltham, MA, USA). The specific surface area was quantified using a multipoint Brunauer–Emmett–Teller (BET, Conta NOVE-1000 e, Quantachrome Instruments, USA). The UV–vis diffuse reflectance spectra (DRS) were obtained by a TU-1901 (Beijing, China) with a wavelength range of from 200 to 800 nm.

2.4. Measurement of Photocatalyst Activity

The photocatalytic performance of g-C₃N₄ samples was evaluated in terms of degrading the SMZ under a 500 W xenon lamp with a 420 nm cut-off filter to simulate visible light irradiation. The distance between the surface of the reaction liquid and the light source was about 10 cm, and then the photocatalyst (100 mg/L) was added to the SMZ solution (3 mg/L) to make a final volume of 50 mL. After ultrasonic treatment for 5 min, the dispersed solution was subjected to gentle stirring for 30 min under dark conditions to reach adsorption–desorption equilibrium. A 1.5 mL suspension was withdrawn and filtered through a 0.22 µm filter (Millipore) at fixed internal time intervals. The SMZ concentration was measured by HPLC (Agilent Technologies 1200-Series).

The photocatalytic degradation process can be transformed to pseudo-first-order kinetics (Equation (1)) through data fitting; thus, pseudo-first-order reaction kinetics (k) can be used to compare the photodegradation efficiency of photocatalyst samples under the same conditions [47,48]:

$$\ln(C_0/C_t) = kt \quad (1)$$

3. Results and Discussion

3.1. Characterization

The morphologies and microstructures of the g-C₃N₄ samples were investigated by SEM, as shown in Figure 1. It can be seen from Figure 1a–c that the surface of g-C₃N₄ samples exfoliated by the thermal oxidative method had a large number of irregular blocky agglomerates, and the size distribution was mainly in the range of several micrometers, owing to the existence of the O element, which will produce H₂O gas during the high-temperature calcination process. Then, the escaping H₂O gas acts as soft templates to help inorganic nanocrystals form porous micro-structures [30,31,42,44]. As thiourea were used as precursors, H₂S gas was produced and acted as soft templates to change the microstructure, resulting in the g-C₃N₄ sample microstructure being different, as shown in Figure 1j–l [42]. When melamine and dicyandiamide were used as precursors, there was no obvious pore structure on the surface of the g-C₃N₄ samples (Figure 1d–i), which may be attributed to the NH₃ generated during the high-temperature calcination not reacting with other gases. It revealed that the release of NH₃ remained constant, resulting in a better quality of the produced g-C₃N₄ samples. Specifically, these samples had a higher degree of polymerization and crystallinity. As shown in Figure 1, it was found that the bulk g-C₃N₄ samples were exfoliated more intensively with the increase of thermal oxidative etching time, and the surfaces demonstrated more wrinkles and irregular shapes. At the same time, with the increase of thermal oxidative etching time, the g-C₃N₄ nanosheets became very thin, and some of the nanosheets tended to break, in that many smaller nanosheets were produced, and the agglomeration phenomenon was improved.

The XRD patterns of g-C₃N₄ samples synthesized from the four different precursors are shown in Figure 2. Two typical diffraction peaks were observed in the XRD patterns for all samples, indicating the successful synthesis of g-C₃N₄ by thermal oxidative etching of the four different precursors. A minor angle diffraction peak at 13.0° can be attributed to an in-planar structural packing, which corresponded to (100) crystal planes of g-C₃N₄, and the strong peak at 27.4° accorded with the repeated the inter-layer stacking of conjugated aromatic systems, which was indexed for graphitic materials as the (002) peak [49–51]. The XRD patterns of all samples did not have significant difference at 13.0°, corresponding to diffraction from (100) planes. Meanwhile, the interplane distance of all samples was around 0.68 nm, which is consistent with the other literature [52,53]. The XRD patterns of U0, M0, D0 and T0 showed diffraction peak intensity around 27.4°: M0 > D0 > T0 > U0, indicating the presence of smaller crystalline domains in U0, in line with the SEM observation. In addition, at the same peak positions, these patterns displayed a slight broadening width of the overall peaks following longer thermal oxidative etching time, indicating that the crystallinity of the g-C₃N₄ decreased at prolonging thermal oxidative etching time and more edge defects were thereupon made. Hence, the interlayer spacing of g-C₃N₄ material

became larger, which is in good agreement with the phenomenon observed by SEM. The average crystallite size of all samples is shown in Table 1. The crystalline size of g-C₃N₄ that used urea as a precursor was the smallest, and the thermal oxidation etching time had no obvious effect on the crystalline size.

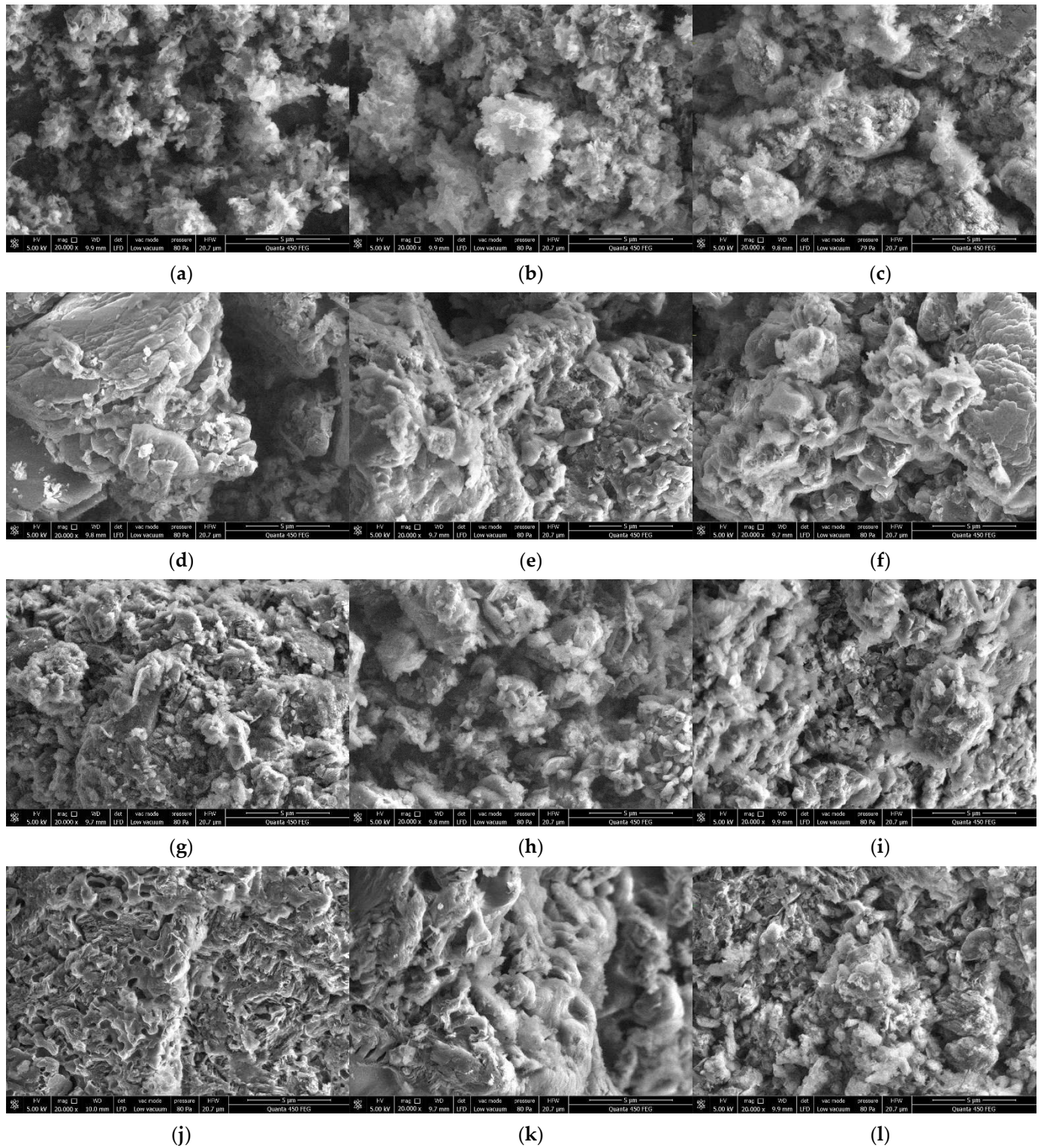


Figure 1. SEM images of all g-C₃N₄ samples: (a) U0, (b) U165, (c) U330, (d) M0, (e) M165, (f) M330, (g) D0, (h) D165, (i) D330, (j) T0, (k) T165 and (l) T330.

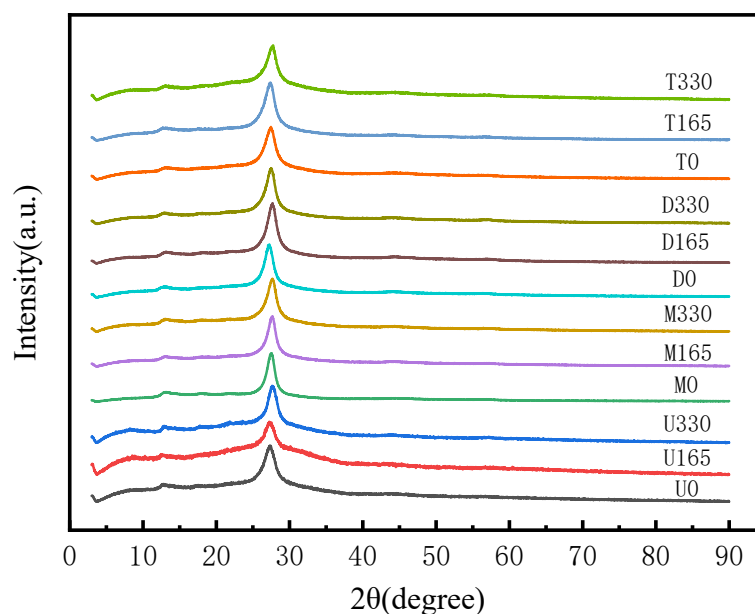


Figure 2. XRD patterns of all $g\text{-C}_3\text{N}_4$ samples.

Table 1. The average crystallite size of 12 kinds of $g\text{-C}_3\text{N}_4$.

Sample	Size (nm)
U0	3.1
U165	2
U330	3.9
M0	5.6
M165	5.1
M330	4.5
D0	5.8
D165	5
D330	7.5
T0	6.5
T165	3.9
T330	3.4

The FTIR spectra indicates the functional groups of the $g\text{-C}_3\text{N}_4$ samples presented in Figure 3. Similar FTIR spectral vibration modes of $g\text{-C}_3\text{N}_4$ samples from different precursors display a similar characteristic IR absorption spectrum. They show several major bands centered at about 810, 1200–1700 and 3200–3400 cm^{-1} . The sharp peak at 810 cm^{-1} originates from the characteristic breathing mode of s-triazine [54–56]. The peaks in the region from 1200 to 1700 cm^{-1} are the typical stretching vibrations of trigonal C–N(–C)–C or bridging C–N(–H)–C heterocycles associated with skeletal stretching vibrations of aromatic rings [57]. The broad peaks between 3200 and 3400 cm^{-1} are assigned to the O–H stretches, indicating that there are adsorbed hydroxyl groups on the $g\text{-C}_3\text{N}_4$ sample surfaces [58,59]. The similarity among all the bands suggests that the thermal treatment of the $g\text{-C}_3\text{N}_4$ samples does not bring about significant changes in the structure of the $g\text{-C}_3\text{N}_4$ nanosheets.

To investigate the surface composition and chemical state of U330, XPS was carried out, and the results are shown in Figure 4. For the sake of brevity, only carbon, nitrogen, oxygen and sodium were detected in the XPS spectra. The strength of the N1s intensity was strongest owing to its highest proportion in U330. The O1s peak can be attributed to the adsorbed H_2O on the sample surface, which appeared at about 532.3 eV. To further observe the chemical bonding among nitrogen, carbon and oxygen atoms in U330, the high-definition C1s, N1s and O1s spectra were further deconvoluted into Gaussian–Lorentzian peaks, respectively. As shown in Figure 4b, the C1s spectra show three peaks, in which

the peak centered at 284.8 eV is attributed to the sp^2 hybridized C atoms C-C [30,60], at 286.2 eV is identified as C=O [61,62] and at 288.2 eV originated from the sp^2 bonded C in $N=C(-N)_2$ [63,64]. The high-definition N1s spectra can also be deconvoluted into three Gaussian–Lorentzian peaks (Figure 4c) centered at about 398.8, 400.1 and 401.2 eV, respectively. The peak at 398.8 eV is assigned to aromatic N bonded to two C ($C=N-C$) sp^2 bonded C= $N-C$ involved in the triazine rings or heptazine rings [65–67]. The peak 400.1 eV is typically attributed to the graphite-like N in the form of the sp^2 hybridized N bonded to three atoms ($C-N(-C)-C$ or $C-N(-H)-C$) [30]. Additionally, the peak 401.2 eV is ascribed to the sp^3 hybridized terminal N ($N-H_2$ or $N-O$) of the heptazine rings [30,68]. In addition, the spectrum of O1s in Figure 4d can be deconvoluted into two single peaks with binding energies of 531.3 and 533.6 eV, which ascribed to carbonyl C=O group and adsorbed water [66], respectively. This was also confirmed by FTIR.

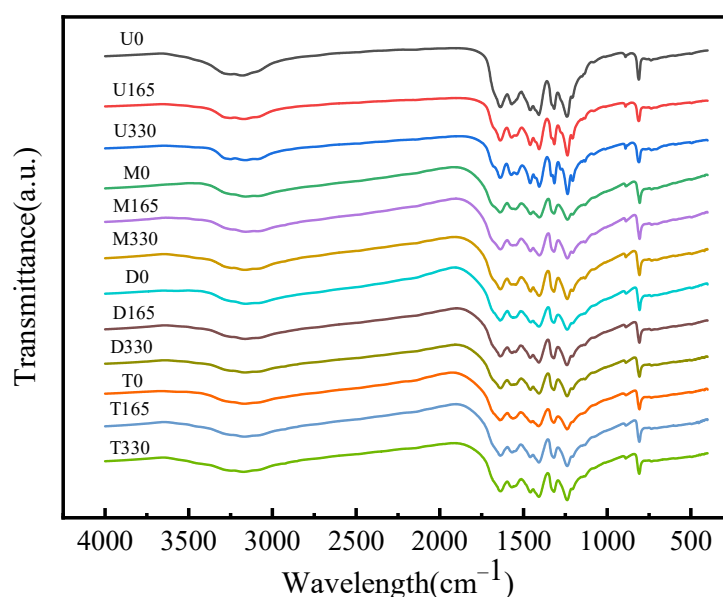


Figure 3. FT-IR spectra of all $g-C_3N_4$ samples.

The obtained specific BET surface areas of all $g-C_3N_4$ samples are summarized in Table 2. From Table 2, the results indicate that the specific BET surface area increased with prolonging thermal oxidative etching time. Additionally, the larger surface area could provide more reactive sites and adsorb more reactants, which can enhance the photocatalyst activity of samples. Furthermore, the average pore volume also increased with the extension of thermal oxidative etching time, which can be attributed to the mesopores originating from the stacking of $g-C_3N_4$ nanosheets. These variation tendencies further confirm that the bulk $g-C_3N_4$ can be effectively exfoliated by extension of thermal oxidative etching time, which is also consistent with SEM. Meanwhile, urea-derived $g-C_3N_4$ nanosheets had the largest specific surface area compared to $g-C_3N_4$ derived from other precursors under the same experimental conditions. Elemental analysis results of the prepared samples are given in Table 3. The molar ratios of C to N of all the $g-C_3N_4$ are around 0.60 (theoretical value of $g-C_3N_4 = 0.75$), implying incomplete crystallization.

The PL emission spectra of $g-C_3N_4$ samples that used urea as a precursor were recorded in Figure 5. PL were used to understand the efficiency of trapping, migration, transfer and separation of charge carriers, and to investigate their lifetime in semiconductors, since PL emission results from the recombination of electron/hole pairs [69,70]. In general, a lower PL intensity suggests a lower recombination rate of the electron–hole pairs under light irradiation [71–73]. It can be seen from Figure 5 that all the samples show a broad PL emission spectra in the 500–580 nm region. In comparison, it can be observed that U330 exhibits the lowest emission intensity, which means that U330 is more efficient at

promoting the separation of electron–hole pairs. This indicates that U330 is preferable in the case of utilizing the materials as catalysts in the photoreactions, and also suggests that the separation efficiency of photogenerated electrons and holes in urea-derived $g\text{-C}_3\text{N}_4$ samples increases with the extension of thermal etching time.

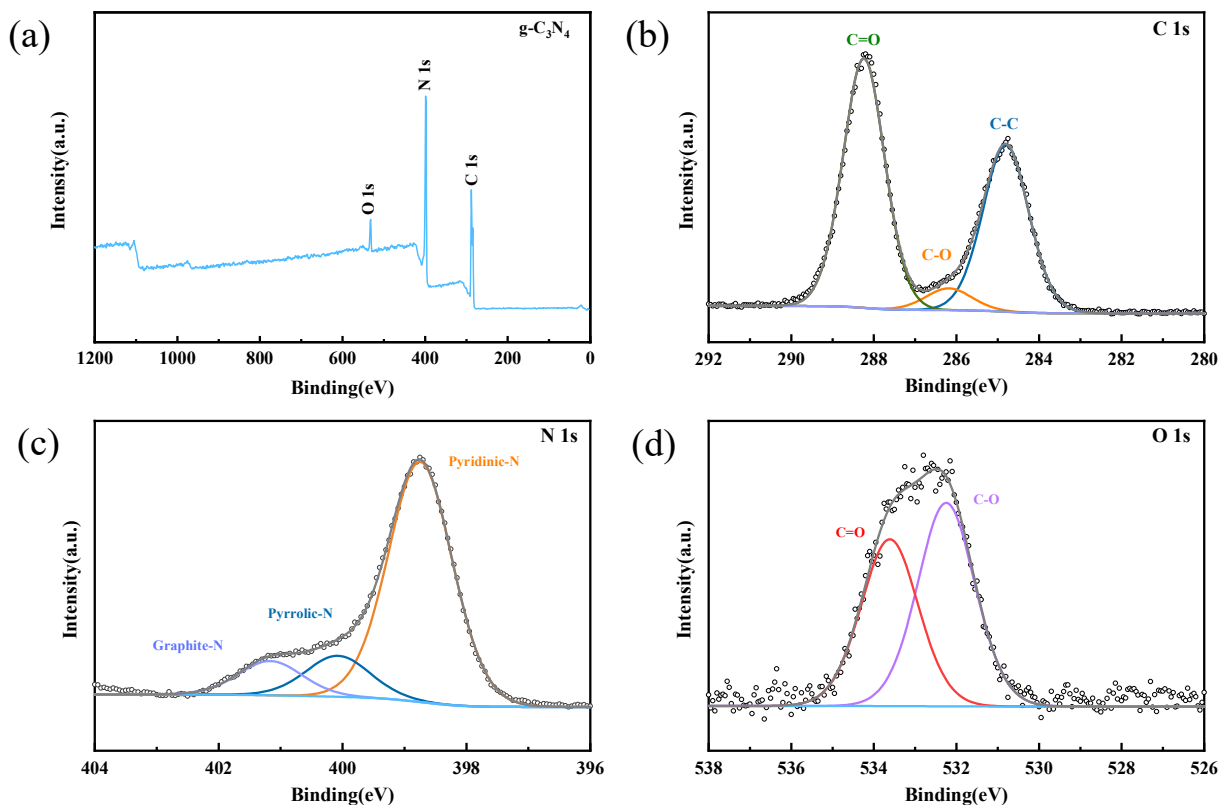


Figure 4. XPS spectra of U330: (a) full spectrum of U330, (b) C1s, (c) N1s and (d) O1s.

Table 2. BET analysis of 12 kinds of $g\text{-C}_3\text{N}_4$.

Samples	Specific Surface Area (m ² /g)	Average Pore Size (nm)	Pore Volume (cm ³ /g)
U0	63.464	3.845	0.333
U165	112.596	3.866	0.385
U330	160.735	3.822	0.794
M0	10.585	3.850	0.067
M165	46.179	3.853	0.191
M330	75.610	3.854	0.300
D0	6.050	3.775	0.028
D165	37.116	3.821	0.145
D330	96.931	3.857	0.395
T0	13.381	3.769	0.066
T165	33.366	3.789	0.179
T330	79.759	3.773	0.379

From Figure 6, which shows the UV–vis of U330, it can be seen that the absorption edge of U330 is about 438 nm, indicating that U330 is responsive in the visible light range and can be activated by visible light, which may be attributed to the bulk $g\text{-C}_3\text{N}_4$ nanosheets with different structures and morphology after thermal etching. At the same time, the thickness and size decrease, and the corresponding band gap changes from 2.7 eV to 2.96 eV. Due to the influence of quantum confinement, the red shift of the spectrum is caused and the conduction band and valence band positions move in the opposite direction, which

increases the band gap, enhances the redox ability of photogenerated electron hole pairs, and improves the photocatalytic activity of the synthesized samples.

Table 3. Elemental analysis of 12 kinds of g-C₃N₄.

Sample	C (wt.%)	N (wt.%)	C/N Molar Ratio
U0	37.076	61.634	0.602
U165	37.266	61.153	0.609
U330	37.557	61.547	0.610
M0	36.896	63.443	0.582
M165	36.684	62.081	0.591
M330	36.242	61.708	0.587
D0	37.258	63.082	0.591
D165	36.109	61.482	0.587
D330	36.073	60.711	0.594
T0	36.462	61.766	0.590
T165	36.685	60.603	0.605
T330	36.256	61.366	0.591

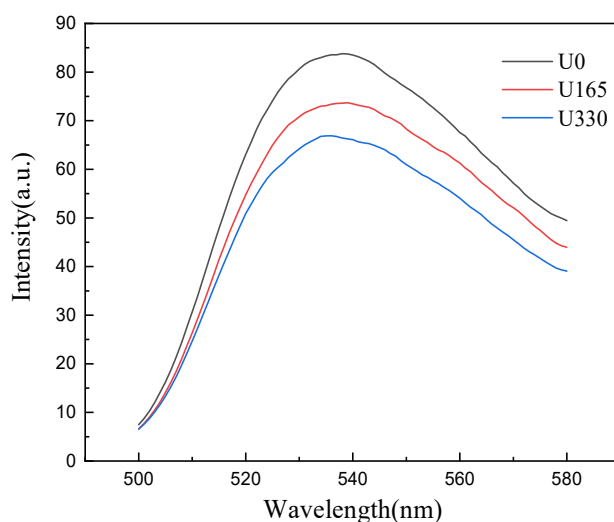


Figure 5. PL spectra of U0, U165 and U330.

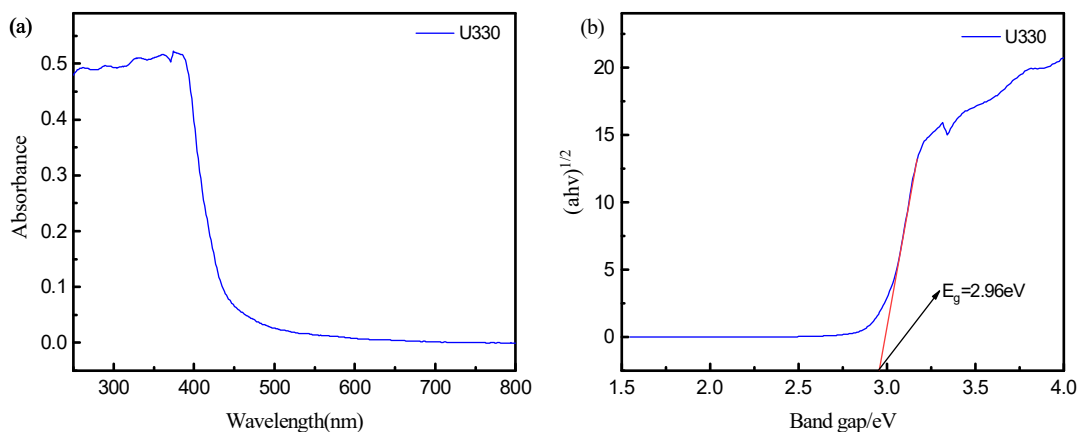


Figure 6. UV-vis diffuse reflectance absorption spectrum of U330: (a) ultraviolet diffuse reflectance spectrum of U330 and (b) energy band spectrum of U330.

3.2. Photocatalyst Performance Analysis

The photocatalytic degradation performance of the synthesized samples was evaluated using degradation of SMZ under visible light and recorded by HPLC, as depicted in Figure 7.

Among these samples, U330, M330, D330 and T330 exhibited dramatically enhanced visible light photocatalytic activity than the bulk $g\text{-C}_3\text{N}_4$ samples synthesized from different precursors. Kinetic analysis showed that the photodegradation of SMZ followed first-order kinetics, and the kinetic constants (k) were shown as Figure 7b and Table 4. The rate constants of U330, M330, D330 and T330 were 1.57, 2.04, 3.36 and 3.69 times for the corresponding bulk of $g\text{-C}_3\text{N}_4$, respectively. This finding further confirms that the photocatalytic performance could be enhanced by an increase in thermal oxidative etching time. Thermal oxidative etching leads to a significant enhancement of the photocatalytic activity of $g\text{-C}_3\text{N}_4$, mainly due to its thin conjugated structure with a larger surface area and porous structure, which provides the surface with more active sites for promoting adsorption and more channels for mass transfer. Additionally, this is also in line with the BET analysis results. Among these samples, U330 exhibited the most photocatalytic activity for SMZ under the simulated visible sunlight, whose rate constants were 2.14, 1.47 and 1.40 times for M330, D330 and T330, respectively. Among all the photocatalysts from different precursors, U330 was found to be the best one. This might be caused by several factors. Firstly, U330 had enhanced photoactivity due to being less condensed and porous, as confirmed by SEM, leading to a higher BET area and larger proportion of macropores; both allow better mass transport under lower diffusion resistance, enabling molecules to be transferred more easily in the photocatalyst process. Secondly, the urea precursor undergoes a series of gas-releasing stages to form melamine, leading to the formation of a less condensed and porous $g\text{-C}_3\text{N}_4$ with more edge-excited amino groups, compared to other precursors. The substrate could be activated by terminal uncondensed amino groups of the defective U330 structures via O–H bonding and nucleophilic attack [45,74,75]. Hence, U330 is the best choice to be applied to the photodegradation of sulfonamides in water under visible light.

Table 4. Kinetic fitting parameters of photodegradation kinetics of SMZ by $g\text{-C}_3\text{N}_4$ prepared from different precursors under visible light.

Samples	K (min^{-1})
U0	0.01296
U165	0.01592
U330	0.02039
M0	0.00465
M165	0.00665
M330	0.00953
D0	0.00414
D165	0.00951
D330	0.0139
T0	0.00394
T165	0.01355
T330	0.01455

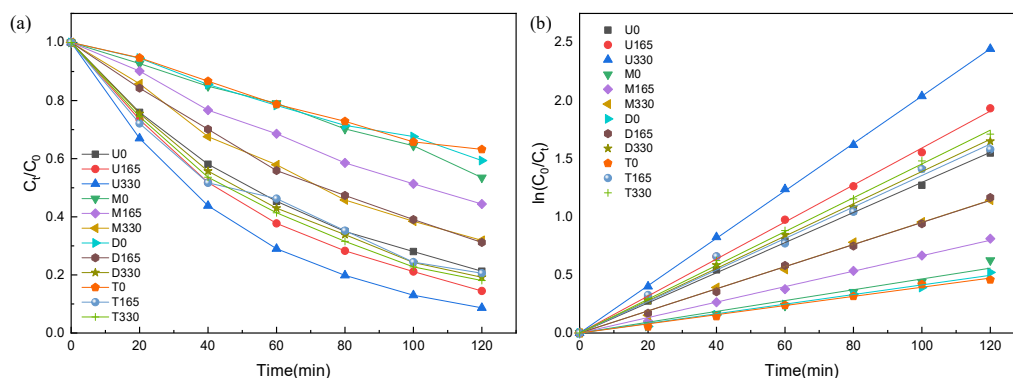


Figure 7. Photocatalytic efficiencies of SMZ by different $g\text{-C}_3\text{N}_4$ under visible light: (a) t degradation curve; (b) degradation kinetics.

4. Conclusions

In summary, the g-C₃N₄ nanosheets were synthesized through the thermal oxidative etching method with two different heating times and from four different precursors. The results from characterizations and photocatalytic evaluations showed that thermal oxidative etching time has a significant effect on the properties of g-C₃N₄, including crystallinity, polymerization degree, surface area and photocatalytic activity. As the heating time increased, the g-C₃N₄ samples showed lower crystallinity, a higher degree of polymerization, a larger number of macropores and a more enhanced photocatalytic performance. In addition, the type of precursors also significantly affected the photocatalytic performance of the g-C₃N₄ samples. The kinetic analysis revealed that the photodegradation of SMZ followed first-order kinetics and the rate constant of U330 was 2.14 times that of M330, 1.47 times that of D330 and 1.40 times that of T330. These results indicate that U330 has the potential to be a promising photocatalyst for the degradation of sulfonamides in the aquatic environment due to its superior photodegradation performance and the advantages of its porous and less condensed structure. All these factors prove that U330 is an excellent promising photocatalyst for the degradation of sulfonamides in the aquatic environment.

Author Contributions: Conceptualization, K.L., M.C. and L.C.; methodology, W.X., S.Z. and Y.H.; software, M.C. and W.X.; investigation, M.C., W.X., S.Z. and Z.H.; resources, K.L. and L.C.; data curation, K.L.; writing—original draft preparation, K.L., M.C., and W.X.; writing—review and editing, K.L. and L.C.; visualization, Y.H.; supervision, K.L. and L.C.; funding acquisition, K.L. and L.C. All authors have read and agreed to the published version of the manuscript.

Funding: This research was funded by the National Natural Science Foundation of China (51878316) and the Science and Technology Research Planning Project of Jilin Provincial Department of Education (JJKH20220297KJ, JJKH20220279KJ).

Institutional Review Board Statement: Not applicable.

Informed Consent Statement: Not applicable.

Data Availability Statement: Not applicable.

Acknowledgments: All authors thank the editor and anonymous reviewers for their constructive comments and suggestions to improve the quality of this paper.

Conflicts of Interest: The authors declare no conflict of interest. The funders had no role in the design of the study; in the collection, analyses, or interpretation of data; in the writing of the manuscript; or in the decision to publish the results.

References

1. Cook, M.A.; Wright, G.D. The past, present, and future of antibiotics. *Sci. Transl. Med.* **2022**, *14*, eabo7793. [[CrossRef](#)]
2. Wertheimer, A. The urgent need for new antibiotics. *J. Pharm. Health Serv. Res.* **2022**, *13*, 167. [[CrossRef](#)]
3. Ahmed, H.; Zolfo, M.; Williams, A.; Ashubwe-Jalemba, J.; Tweya, H.; Adeapena, W.; Labi, A.K.; Adomako, L.A.B.; Addico, G.N.D.; Banu, R.A.; et al. Antibiotic-Resistant Bacteria in Drinking Water from the Greater Accra Region, Ghana: A Cross-Sectional Study, December 2021–March 2022. *Int. J. Environ. Res. Public Health* **2022**, *19*, 12300. [[CrossRef](#)]
4. Zhang, T.; Li, B. Occurrence, Transformation, and Fate of Antibiotics in Municipal Wastewater Treatment Plants. *Crit. Rev. Environ. Sci. Technol.* **2011**, *41*, 951–998. [[CrossRef](#)]
5. Matamoros, V.; Casas, M.E.; Pastor, E.; Tadic, D.; Canameras, N.; Carazo, N.; Bayona, J.M. Effects of tetracycline, sulfonamide, fluoroquinolone, and lincosamide load in pig slurry on lettuce: Agricultural and human health implications. *Environ. Res.* **2022**, *215*, 114237. [[CrossRef](#)]
6. Xia, W.K.; Liu, C.; Ye, S.; Wang, L.; Liu, R.Y. Synthesis of A Sulfonamide-Substituted Benzothiadiazole-Based Fluorescent Dye and Study of Its Application for Long-Term Cancer Cell Tracking. *Chin. J. Org. Chem.* **2022**, *42*, 2535–2541. [[CrossRef](#)]
7. Yan, X.J.; Liu, W.W.; Wen, S.F.; Wang, L.J.; Zhu, L.S.; Wang, J.; Kim, Y.M.; Wang, J.H. Effect of sulfamethazine on the horizontal transfer of plasmid-mediated antibiotic resistance genes and its mechanism of action. *J. Environ. Sci.* **2023**, *127*, 399–409. [[CrossRef](#)]
8. Li, Y.; Liu, H.L.; Xing, W.M.; Wang, J.; Fan, H.Y. Effects of irrigation water quality on the presence of pharmaceutical and personal care products in topsoil and vegetables in greenhouses. *Environ. Sci. Pollut. Res.* **2022**, *30*, 13726–13738. [[CrossRef](#)]
9. Sun, Q.; Sun, Y.; Zhou, M.Y.; Cheng, H.M.; Chen, H.Y.; Dorus, B.; Lu, M.; Le, T. A 2D/3D g-C₃N₄/ZnO heterojunction enhanced visible-light driven photocatalytic activity for sulfonamides degradation. *Ceram. Int.* **2022**, *48*, 7283–7290. [[CrossRef](#)]

10. Cui, J.; Fu, L.F.; Tang, B.; Bin, L.Y.; Li, P.; Huang, S.S.; Fu, F.L. Occurrence, ecotoxicological risks of sulfonamides and their acetylated metabolites in the typical wastewater treatment plants and receiving rivers at the Pearl River Delta. *Sci. Total Environ.* **2020**, *709*, 136192. [[CrossRef](#)]
11. Garcia-Galan, M.J.; Blanco, S.G.; Roldan, R.L.; Diaz-Cruz, S.; Barcelo, D. Ecotoxicity evaluation and removal of sulfonamides and their acetylated metabolites during conventional wastewater treatment. *Sci. Total Environ.* **2012**, *437*, 403–412. [[CrossRef](#)]
12. Sannino, F.; Pansini, M.; Marocco, A.; Cinquegrana, A.; Esposito, S.; Tammaro, O.; Barrera, G.; Tiberto, P.; Allia, P.; Pirozzi, D. Removal of sulfanilamide by tailor-made magnetic metal-ceramic nanocomposite adsorbents. *J. Environ. Manag.* **2022**, *310*, 114701. [[CrossRef](#)]
13. Shehzad, H.; Farooqi, Z.H.; Ahmed, E.; Sharif, A.; Razzaq, S.; Mirza, F.N.; Irfan, A.; Begum, R. Synthesis of hybrid biosorbent based on 1,2-cyclohexylenedinitrilotetra-acetic acid modified crosslinked chitosan and organo-functionalized calcium alginate for adsorptive removal of Cu(II). *Int. J. Biol. Macromol.* **2022**, *209*, 132–143. [[CrossRef](#)]
14. Baran, W.; Adamek, E.; Jajko, M.; Sobczak, A. Removal of veterinary antibiotics from wastewater by electrocoagulation. *Chemosphere* **2018**, *194*, 381–389. [[CrossRef](#)]
15. Xie, T.T.; Chen, K.; Xie, H.X.; Miao, C.C.; Yu, M.; Li, F.Y.; Chen, Y.H.; Yang, X.J.; Li, P.; Niu, Q.S. Highly negatively charged nanofiltration membrane prepared with a novel diamino-sulfonamide aqueous monomer for efficient removal of anionic dyes. *Appl. Surf. Sci.* **2022**, *599*, 153914. [[CrossRef](#)]
16. Aber, S.; Ghalamchi, L.; Hosseinzadeh, H.; Nofouzi, K.; Naseri, A. Biological treatment of ranitidine and cefixime trihydrate mixed solution by activated sludge in sequencing batch reactor. *Desalination Water Treat.* **2021**, *225*, 94–103. [[CrossRef](#)]
17. Begum, R.; Farooqi, Z.H.; Xiao, J.L.; Ahmed, E.; Sharif, A.; Irfan, A. Crosslinked polymer encapsulated palladium nanoparticles for catalytic reduction and Suzuki reactions in aqueous medium. *J. Mol. Liq.* **2021**, *338*, 116780. [[CrossRef](#)]
18. Naseem, K.; Begum, R.; Wu, W.; Irfan, A.; Nisar, J.; Azam, M.; Farooqi, Z.H. Core/shell composite microparticles for catalytic reduction of p-nitrophenol: Kinetic and thermodynamic study. *Int. J. Environ. Sci. Technol.* **2021**, *18*, 1809–1820. [[CrossRef](#)]
19. Azhar, M.R.; Abid, H.R.; Sun, H.; Periasamy, V.; Tade, M.O.; Wang, S. Excellent performance of copper based metal organic framework in adsorptive removal of toxic sulfonamide antibiotics from wastewater. *J. Colloid Interface Sci.* **2016**, *478*, 344–352. [[CrossRef](#)]
20. Zhang, S.X.; Pang, X.F.; Yue, Z.; Zhou, Y.H.; Duan, H.T.; Shen, W.J.; Li, J.F.; Liu, Y.L.; Cheng, Q.P. Sulfonamides removed from simulated livestock and poultry breeding wastewater using an in-situ electro-Fenton process powered by photovoltaic energy. *Chem. Eng. J.* **2020**, *397*, 125466. [[CrossRef](#)]
21. Liang, C.Y.; Wei, D.; Zhang, S.Y.; Ren, Q.H.; Shi, J.P.; Liu, L. Removal of antibiotic resistance genes from swine wastewater by membrane filtration treatment. *Ecotoxicol. Environ. Saf.* **2021**, *210*, 111885. [[CrossRef](#)]
22. Yu, Z.H.; Zhang, X.B.; Ngo, H.H.; Guo, W.S.; Wen, H.T.; Deng, L.J.; Li, Y.J.; Guo, J.B. Removal and degradation mechanisms of sulfonamide antibiotics in a new integrated aerobic submerged membrane bioreactor system. *Bioresour. Technol.* **2018**, *268*, 599–607. [[CrossRef](#)]
23. Li, X.T.; Liang, K.M.; Yang, B.; Xiao, K.; Duan, H.B.; Song, G.Q.; Zhao, H.Z. Preparation and application of a targeted magnetically separated catalyst for sulfonamides degradation based on molecular dynamics selection and mechanism analysis. *Chem. Eng. J.* **2022**, *432*, 134365. [[CrossRef](#)]
24. Gan, W.; Fu, X.C.; Guo, J.; Zhang, M.; Li, D.D.; Ding, C.S.; Lu, Y.Q.; Wang, P.; Sun, Z.Q. Ag nanoparticles decorated 2D/2D TiO₂/g-C₃N₄ heterojunction for efficient removal of tetracycline hydrochloride: Synthesis, degradation pathways, and mechanism. *Appl. Surf. Sci.* **2022**, *606*, 154837. [[CrossRef](#)]
25. Gong, Y.A.; Wang, Y.; Tang, M.M.; Zhang, H.; Wu, P.; Liu, C.J.; He, J.; Jiang, W. A two-step process coupling photocatalysis with adsorption to treat tetracycline—Copper(II) hybrid wastewaters. *J. Water Process Eng.* **2022**, *47*, 102710. [[CrossRef](#)]
26. Hao, B.F.; Guo, J.P.; Zhang, L.; Ma, H.Z. Magnetron sputtered TiO₂/CuO heterojunction thin films for efficient photocatalysis of Rhodamine B. *J. Alloys Compd.* **2022**, *903*, 163851. [[CrossRef](#)]
27. Song, Y.L.; Qi, J.Y.; Tian, J.Y.; Gao, S.S.; Cui, F.Y. Construction of Ag/g-C₃N₄ photocatalysts with visible-light photocatalytic activity for sulfamethoxazole degradation. *Chem. Eng. J.* **2018**, *341*, 547–555. [[CrossRef](#)]
28. Yang, Y.X.; Guo, Y.N.; Liu, F.Y.; Yuan, X.; Guo, Y.H.; Zhang, S.Q.; Guo, W.; Huo, M.X. Preparation and enhanced visible-light photocatalytic activity of silver deposited graphitic carbon nitride plasmonic photocatalyst. *Appl. Catal. B-Environ.* **2013**, *142*, 828–837. [[CrossRef](#)]
29. Zhang, F.J.; Xie, F.Z.; Zhu, S.F.; Liu, J.; Zhang, J.; Mei, S.F.; Zhao, W. A novel photofunctional g-C₃N₄/Ag₃PO₄ bulk heterojunction for decolorization of Rh. *B. Chem. Eng. J.* **2013**, *228*, 435–441. [[CrossRef](#)]
30. Liu, J.H.; Zhang, T.K.; Wang, Z.C.; Dawson, G.; Chen, W. Simple pyrolysis of urea into graphitic carbon nitride with recyclable adsorption and photocatalytic activity. *J. Mater. Chem.* **2011**, *21*, 14398–14401. [[CrossRef](#)]
31. Dong, J.Q.; Zhang, Y.; Hussain, M.I.; Zhou, W.J.; Chen, Y.Z.; Wang, L.N. g-C₃N₄: Properties, Pore Modifications, and Photocatalytic Applications. *Nanomaterials* **2022**, *12*, 121. [[CrossRef](#)]
32. Mahmood, A.; Irfan, A.; Wang, J.L. Molecular level understanding of the chalcogen atom effect on chalcogen-based polymers through electrostatic potential, non-covalent interactions, excited state behaviour, and radial distribution function. *Polym. Chem.* **2022**, *13*, 5993–6001. [[CrossRef](#)]
33. Mahmood, A.; Abdullah, M.I.; Nazar, M.F. Quantum Chemical Designing of Novel Organic Non-Linear Optical Compounds. *Bull. Korean Chem. Soc.* **2014**, *35*, 1391–1396. [[CrossRef](#)]

34. Mahmood, A.; Khan, S.U.D.; Rehman, F.U. Assessing the quantum mechanical level of theory for prediction of UV/Visible absorption spectra of some aminoazobenzene dyes. *J. Saudi Chem. Soc.* **2015**, *19*, 436–441. [[CrossRef](#)]
35. Mou, Z.G.; Chen, T.; Tao, Y.; Gao, Y.; Sun, J.H.; Lei, W.I. Fabrication of g-C₃N₄/N,Fe co-doped CQDs composites: In situ decoration of g-C₃N₄ with N-CQDs and Fe and efficient visible-light photocatalytic degradation of tetracycline. *J. Phys. D-Appl. Phys.* **2022**, *55*, 444005. [[CrossRef](#)]
36. Xia, X.; Xu, B.G.; Zhang, H.Y.; Ji, K.; Ji, X.S.; Wang, D.; Yang, P. NiCoP/g-C₃N₄ Schottky heterojunctions towards efficient photocatalytic NO oxidation. *J. Alloys Compd.* **2022**, *928*, 167207. [[CrossRef](#)]
37. Zhou, Y.Y.; Zhang, J.X.; Wu, D.F. Enhanced photocatalytic degradation of ciprofloxacin over Bi₂MoO₆/g-C₃N₄/BiFeO₃ heterojunction photocatalyst under visible light irradiation. *Mater. Sci. Semicond. Process* **2022**, *151*, 453–461. [[CrossRef](#)]
38. Wang, L.; Wang, Z.L.; Wang, F.; Guan, Y.; Meng, D.; Li, X.; Zhou, H.Z.; Li, X.D.; Chen, Y.W.; Tan, Z.L. Response of performance, antibiotic resistance genes and bacterial community exposure to compound antibiotics stress: Full nitrification to shortcut nitrification and denitrification. *Chem. Eng. J.* **2023**, *451*, 107011. [[CrossRef](#)]
39. Putri, L.K.; Ng, B.J.; Er, C.C.; Ong, W.J.; Chang, W.S.; Mohamed, A.R.; Chai, S.P. Insights on the impact of doping levels in oxygen-doped gC(3)N(4) and its effects on photocatalytic activity. *Appl. Surf. Sci.* **2020**, *504*, 144427. [[CrossRef](#)]
40. Yan, W.; Yan, L.; Jing, C.Y. Impact of doped metals on urea-derived g-C₃N₄ for photocatalytic degradation of antibiotics: Structure, photoactivity and degradation mechanisms. *Appl. Catal. B-Environ.* **2019**, *244*, 475–485. [[CrossRef](#)]
41. Li, H.P.; Liu, J.Y.; Hou, W.G.; Du, N.; Zhang, R.J.; Tao, X.T. Synthesis and characterization of g-C₃N₄/Bi₂MoO₆ heterojunctions with enhanced visible light photocatalytic activity. *Appl. Catal. B-Environ.* **2014**, *160*, 89–97. [[CrossRef](#)]
42. Zhang, Y.W.; Liu, J.H.; Wu, G.; Chen, W. Porous graphitic carbon nitride synthesized via direct polymerization of urea for efficient sunlight-driven photocatalytic hydrogen production. *Nanoscale* **2012**, *4*, 5300–5303. [[CrossRef](#)] [[PubMed](#)]
43. Niu, P.; Zhang, L.; Liu, G.; Cheng, H.M. Graphene-like carbon nitride nanosheets for improved photocatalytic activities. *Adv. Funct. Mater.* **2012**, *22*, 4763–4770. [[CrossRef](#)]
44. Ren, J.; Liu, X.; Zhang, L.; Liu, Q.Q.; Gao, R.H.; Dai, W.L. Thermal oxidative etching method derived graphitic C₃N₄: Highly efficient metal-free catalyst in the selective epoxidation of styrene. *Rsc Adv.* **2017**, *7*, 5340–5348. [[CrossRef](#)]
45. Su, Q.; Sun, J.; Wang, J.Q.; Yang, Z.F.; Cheng, W.G.; Zhang, S.J. Urea-derived graphitic carbon nitride as an efficient heterogeneous catalyst for CO₂ conversion into cyclic carbonates. *Catal. Sci. Technol.* **2014**, *4*, 1556–1562. [[CrossRef](#)]
46. Dong, H.; Guo, X.T.; Yang, C.; Ouyang, Z.Z. Synthesis of g-C₃N₄ by different precursors under burning explosion effect and its photocatalytic degradation for tylosin. *Appl. Catal. B-Environ.* **2018**, *230*, 65–76. [[CrossRef](#)]
47. Hu, J.Y.; Tian, K.; Jiang, H. Improvement of phenol photodegradation efficiency by a combined g-C₃N₄/Fe(III)/persulfate system. *Chemosphere* **2016**, *148*, 34–40. [[CrossRef](#)] [[PubMed](#)]
48. Yan, S.C.; Li, Z.S.; Zou, Z.G. Photodegradation of Rhodamine B and Methyl Orange over Boron-Doped g-C₃N₄ under Visible Light Irradiation. *Langmuir* **2010**, *26*, 3894–3901. [[CrossRef](#)]
49. Meftahi, A.; Shabani-Nooshabadi, M.; Reisi-Vanani, A. AgI/g-C₃N₄ nanocomposite as electrode material for supercapacitors: Comparative study for its efficiency in three different aqueous electrolytes br. *Electrochim. Acta* **2022**, *430*, 141052. [[CrossRef](#)]
50. Danish, M.; Athar, M.S.; Ahmad, I.; Warshagha, M.Z.A.; Rasool, Z.; Muneer, M. Highly efficient and stable Fe₂O₃/g-C₃N₄/GO nanocomposite with Z-scheme electron transfer pathway: Role of photocatalytic activity and adsorption isotherm of organic pollutants in wastewater. *Appl. Surf. Sci.* **2022**, *604*, 154604. [[CrossRef](#)]
51. Asadi, A.; Daglioglu, N.; Hasani, T.; Farhadian, N. Construction of Mg-doped ZnO/g-C₃N₄@ZIF-8 multi-component catalyst with superior catalytic performance for the degradation of illicit drug under visible light. *Colloids Surf. A-Physicochem. Eng. Asp.* **2022**, *650*, 129536. [[CrossRef](#)]
52. Wu, X.T.; Liu, C.G.; Li, X.F.; Zhang, X.G.; Wang, C.; Liu, Y.K. Effect of morphology on the photocatalytic activity of g-C₃N₄ photocatalysts under visible-light irradiation. *Mater. Sci. Semicond. Process* **2015**, *32*, 76–81. [[CrossRef](#)]
53. Zhong, K.D.; Feng, J.W.; Gao, H.B.; Zhang, Y.M.; Lai, K.R. Fabrication of BiVO₄@g-C₃N₄(100) heterojunction with enhanced photocatalytic visible-light-driven activity. *J. Solid State Chem.* **2019**, *274*, 142–151. [[CrossRef](#)]
54. Zhang, H.; Zhao, L.X.; Geng, F.L.; Guo, L.H.; Wan, B.; Yang, Y. Carbon dots decorated graphitic carbon nitride as an efficient metal-free photocatalyst for phenol degradation. *Appl. Catal. B-Environ.* **2016**, *180*, 656–662. [[CrossRef](#)]
55. Faisal, M.; Ismail, A.A.; Harraz, F.A.; Al-Sayari, S.A.; El-Toni, A.M.; Al-Assiri, M.S. Synthesis of highly dispersed silver doped g-C₃N₄ nanocomposites with enhanced visible-light photocatalytic activity. *Mater. Des.* **2016**, *98*, 223–230. [[CrossRef](#)]
56. Lei, Y.; Huang, J.F.; Li, X.A.; Lv, C.Y.; Hou, C.P.; Liu, J.M. Direct Z-scheme photochemical hybrid systems: Loading porphyrin-based metal-organic cages on graphitic-C₃N₄ to dramatically enhance photocatalytic hydrogen evolution. *Chin. J. Catal.* **2022**, *43*, 2249–2258. [[CrossRef](#)]
57. Bavani, T.; Madhavan, J.; Preeyanghaa, M.; Neppolian, B.; Murugesan, S. Construction of direct Z-scheme g-C₃N₄/BiYWO₆ heterojunction photocatalyst with enhanced visible light activity towards the degradation of methylene blue. *Environ. Sci. Pollut. Res.* **2022**, *30*, 10179–10190. [[CrossRef](#)]
58. Wang, H.; He, W.J.; Dong, X.A.; Wang, H.Q.; Dong, F. In situ FT-IR investigation on the reaction mechanism of visible light photocatalytic NO oxidation with defective g-C₃N₄. *Sci. Bull.* **2018**, *63*, 117–125. [[CrossRef](#)]
59. Li, F.P.; Huang, Y.H.; Gao, C.Y.; Wu, X.Y. The enhanced photo-catalytic CO₂ reduction performance of g-C₃N₄ with high selectivity by coupling CoNiSx. *Mater. Res. Bull.* **2021**, *144*, 111488. [[CrossRef](#)]

60. Liu, Q.; Guo, Y.R.; Chen, Z.H.; Zhang, Z.G.; Fang, X.M. Constructing a novel ternary Fe(III)/graphene/g-C₃N₄ composite photocatalyst with enhanced visible-light driven photocatalytic activity via interfacial charge transfer effect. *Appl. Catal. B-Environ.* **2016**, *183*, 231–241. [[CrossRef](#)]
61. Yang, X.L.; Qian, F.F.; Zou, G.J.; Li, M.L.; Lu, J.R.; Li, Y.M.; Bao, M.T. Facile fabrication of acidified g-C₃N₄/g-C₃N₄ hybrids with enhanced photocatalysis performance under visible light irradiation. *Appl. Catal. B-Environ.* **2016**, *193*, 22–35. [[CrossRef](#)]
62. Lu, C.H.; Zhang, P.; Jiang, S.J.; Wu, X.; Song, S.Q.; Zhu, M.S.; Lou, Z.Z.; Li, Z.; Liu, F.; Liu, Y.H.; et al. Photocatalytic reduction elimination of UO₂²⁺ pollutant under visible light with metal-free sulfur doped g-C₃N₄ photocatalyst. *Appl. Catal. B-Environ.* **2017**, *200*, 378–385. [[CrossRef](#)]
63. Xu, Q.L.; Cheng, B.; Yu, J.G.; Liu, G. Making co-condensed amorphous carbon/g-C₃N₄ composites with improved visible-light photocatalytic H₂-production performance using Pt as cocatalyst. *Carbon* **2017**, *118*, 241–249. [[CrossRef](#)]
64. Meng, Z.; Xie, Y.; Cai, T.W.; Sun, Z.X.; Jiang, K.M.; Han, W.Q. Graphene-like g-C₃N₄ nanosheets/sulfur as cathode for lithium-sulfur battery. *Electrochim. Acta* **2016**, *210*, 829–836. [[CrossRef](#)]
65. Ma, S.L.; Zhan, S.H.; Jia, Y.N.; Shi, Q.; Zhou, Q.X. Enhanced disinfection application of Ag-modified g-C₃N₄ composite under visible light. *Appl. Catal. B-Environ.* **2016**, *186*, 77–87. [[CrossRef](#)]
66. Wei, M.Y.; Gao, L.; Li, J.; Fang, J.; Cai, W.X.; Li, X.X.; Xu, A.H. Activation of peroxymonosulfate by graphitic carbon nitride loaded on activated carbon for organic pollutants degradation. *J. Hazard. Mater.* **2016**, *316*, 60–68. [[CrossRef](#)]
67. Ma, L.T.; Fan, H.Q.; Wang, J.; Zhao, Y.W.; Tian, H.L.; Dong, G.Z. Water-assisted ions in situ intercalation for porous polymeric graphitic carbon nitride nanosheets with superior photocatalytic hydrogen evolution performance. *Appl. Catal. B-Environ.* **2016**, *190*, 93–102. [[CrossRef](#)]
68. Cao, L.; Dai, P.C.; Zhu, L.; Yan, L.T.; Chen, R.H.; Liu, D.D.; Gu, X.; Li, L.J.; Xue, Q.Z.; Zhao, X.B. Graphitic carbon nitride catalyzes selective oxidative dehydrogenation of propane. *Appl. Catal. B-Environ.* **2020**, *262*, 118277. [[CrossRef](#)]
69. Pant, B.; Pant, H.R.; Barakat, N.A.M.; Park, M.; Han, T.H.; Lim, B.H.; Kim, H.Y. Incorporation of cadmium sulfide nanoparticles on the cadmium titanate nanofibers for enhanced organic dye degradation and hydrogen release. *Ceram. Int.* **2014**, *40*, 1553–1559. [[CrossRef](#)]
70. Yamada, Y.; Yano, K.; Xu, Q.A.; Fukuzumi, S. Cu/Co₃O₄ Nanoparticles as Catalysts for Hydrogen Evolution from Ammonia Borane by Hydrolysis. *J. Phys. Chem. C* **2010**, *114*, 16456–16462. [[CrossRef](#)]
71. Saud, P.S.; Pant, B.; Alam, A.M.; Ghouri, Z.K.; Park, M.; Kim, H.Y. Carbon quantum dots anchored TiO₂ nanofibers: Effective photocatalyst for waste water treatment. *Ceram. Int.* **2015**, *41*, 11953–11959. [[CrossRef](#)]
72. Pant, B.; Barakat, N.A.M.; Pant, H.R.; Park, M.; Saud, P.S.; Kim, J.W.; Kim, H.Y. Synthesis and photocatalytic activities of CdS/TiO₂ nanoparticles supported on carbon nanofibers for high efficient adsorption and simultaneous decomposition of organic dyes. *J. Colloid Interface Sci.* **2014**, *434*, 159–166. [[CrossRef](#)] [[PubMed](#)]
73. Shen, T.; Wang, Q.; Guo, Z.Y.; Kuang, J.L.; Cao, W.B. Hydrothermal synthesis of carbon quantum dots using different precursors and their combination with TiO₂ for enhanced photocatalytic activity. *Ceram. Int.* **2018**, *44*, 11828–11834. [[CrossRef](#)]
74. Liang, J.; Zheng, Y.; Chen, J.; Liu, J.; Hulicova-Jurcakova, D.; Jaroniec, M.; Qiao, S.Z. Facile Oxygen Reduction on a Three-Dimensionally Ordered Macroporous Graphitic C₃N₄/Carbon Composite Electrocatalyst. *Angew. Chem. Int. Ed.* **2012**, *51*, 3892–3896. [[CrossRef](#)] [[PubMed](#)]
75. Sun, J.; Zhang, S.J.; Cheng, W.G.; Ren, J.Y. Hydroxyl-functionalized ionic liquid: A novel efficient catalyst for chemical fixation of CO₂ to cyclic carbonate. *Tetrahedron Lett.* **2008**, *49*, 3588–3591. [[CrossRef](#)]

Disclaimer/Publisher’s Note: The statements, opinions and data contained in all publications are solely those of the individual author(s) and contributor(s) and not of MDPI and/or the editor(s). MDPI and/or the editor(s) disclaim responsibility for any injury to people or property resulting from any ideas, methods, instructions or products referred to in the content.